FLORE
Repository istituzionale dell'Università degli Studi di Firenze

# Design and Assessment of a Machine Vision System for Automatic Vehicle Wheel Alignment

Questa è la Versione finale referata (Post print/Accepted manuscript) della seguente pubblicazione:

*Original Citation:*

Design and Assessment of a Machine Vision System for Automatic Vehicle Wheel Alignment / Rocco Furferi; Lapo Governi; Yary Volpe;Monica Carfagni. - In: INTERNATIONAL JOURNAL OF ADVANCED ROBOTIC SYSTEMS. - ISSN 1729-8806. - STAMPA. - 10 (art. 243):(2013), pp. 1-16. [10.5772/55928]

*Availability:*

This version is available at: 2158/789735 since:

*Published version:*

DOI: 10.5772/55928

*Terms of use:*

Open Access

La pubblicazione è resa disponibile sotto le norme e i termini della licenza di deposito, secondo quanto stabilito dalla Policy per l'accesso aperto dell'Università degli Studi di Firenze (https://www.sba.unifi.it/upload/policy-oa-2016-1.pdf)

*Publisher copyright claim:*

(Article begins on next page)

26 September 2024

INTECH
open science | open minds

OPEN ACCESS
ARTICLE

International Journal of Advanced Robotic Systems

# Design and Assessment of a Machine Vision System for Automatic Vehicle Wheel Alignment

Regular Paper

Rocco Furferi[1,*], Lapo Governi[1], Yary Volpe[1] and Monica Carfagni[1]

1 Department of Mechanics and Industrial Technologies, University of Firenze, Italy
* Corresponding author E-mail: rocco.furferi@unifi.it

Received 2 Jul 2012; Accepted 18 Jan 2013

DOI: 10.5772/55928

© 2013 Furferi et al.; licensee InTech. This is an open access article distributed under the terms of the Creative Commons Attribution License (http://creativecommons.org/licenses/by/3.0), which permits unrestricted use, distribution, and reproduction in any medium, provided the original work is properly cited.

Abstract Wheel alignment, consisting of properly checking the wheel characteristic angles against vehicle manufacturers' specifications, is a crucial task in the automotive field since it prevents irregular tyre wear and affects vehicle handling and safety. In recent years, systems based on Machine Vision have been widely studied in order to automatically detect wheels' characteristic angles. In order to overcome the limitations of existing methodologies, due to measurement equipment being mounted onto the wheels, the present work deals with design and assessment of a 3D machine vision-based system for the contactless reconstruction of vehicle wheel geometry, with particular reference to characteristic planes. Such planes, properly referred to as a global coordinate system, are used for determining wheel angles. The effectiveness of the proposed method was tested against a set of measurements carried out using a commercial 3D scanner; the absolute average error in measuring toe and camber angles with the machine vision system resulted in full compatibility with the expected accuracy of wheel alignment systems.

Keywords Machine Vision, Stereovision, Wheel Alignment

## 1. Introduction

In the automotive industry, vehicle quality and safety require the measurement and adjustment of wheel alignment settings, both during manufacture and afterwards, during the life of the vehicle [1].

It is commonly known [2] that motor vehicle wheel alignment consists of correctly checking the wheel characteristic angles against vehicle manufacturers' specifications. Incorrect alignment may result in rapid and irregular tyre wear, and can dramatically affect vehicle handling and safety.

The two most important wheel angles, to be set during wheel alignment, are the toe and camber angles of the front wheels (see Figure 1).

Toe is defined as the symmetric angle that wheel makes with the longitudinal axis of the vehicle observing the vehicle from above (or below) [3]. When a pair of wheels is set so that their leading edges are pointed slightly towards each other, the wheel pair is said to have toe-in; in other words the two planes tangent to the tyre sidewall

(referred to as "wheel planes" from now on) cross in front of the considered axle with respect to the driving direction. If the leading edges point away from each other, the pair is said to have toe-out. Toe settings affect three major areas of performance: tyre wear, straight-line stability and corner entry handling characteristics.

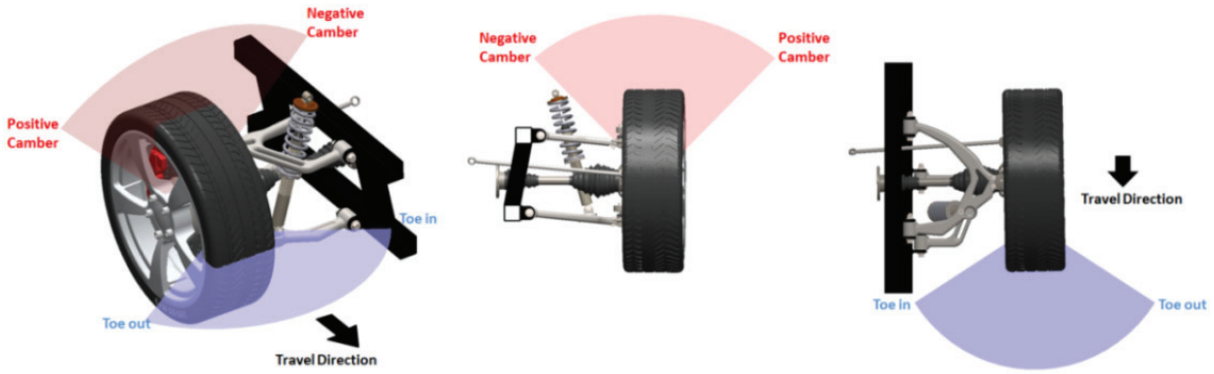


**Figure 1.** Toe and camber angles

Camber is defined as the angle between the vertical axis of the wheels used for steering (i.e., the imaginary line about which the entire assembly of the hub, wheel bearing, rim and tyre rotates when the front wheel turns) and the vertical axis of the vehicle when viewed from the front or rear. If the wheel leans in towards the chassis, it has negative camber; if it leans away from the car, it has positive camber. The cornering force that a tyre can develop is highly dependent on its angle relative to the road surface and so wheel camber has a major effect on the road holding of a car [4].

In the last few decades, the wheel alignment field experienced a tremendous surge of interest, as demonstrated by technical literature. In particular, the state of the art moved from mechanical and electro-mechanical measurement devices, often referred as "direct measurement methods", to 2D and 3D machine vision-based systems.

The earlier direct measurement methods used to be unwieldy, time-consuming, labour-intensive and often less accurate than desired. Dealing with more recent approaches, a number of machine vision-based systems, often referred to as non-contact methods [5], are marketed by companies producing wheel alignment devices, such as Hunter Engineering, Bosch, Beissbarth and John Bean/Snap-on.

Most of modern systems based on artificial vision employ targets, provided with structured markers, to be manually attached on wheel rims; an appositely devised acquisition system is then either placed frontally to the vehicle or placed in a relative lateral position to the vehicle. In the first case [6-9] the structured targets are usually applied to wheels and are provided with a suitable inclination with respect to the wheel plane. The main drawbacks of these systems are:

- the need to position the equipment by attaching it onto the wheel, which often results in a non-trivial procedure and which can expose the equipment to damages from incidental drops, etc.
- the increase in measurement time caused by mounting
- the mounting stability: the targets must be mounted on the wheel with extremely stable connections to prevent generation of measurement errors during movements and rotations of the wheel occurring in the normal measure operations.

In the second case, [10] the targets are placed parallel to the inspected tyre. Then a video camera placed in front of the wheel (i.e., on the side of the vehicle) acquires images of the wheel and of the motion of the structured markers to obtain the characteristic angles. This method can only be applied if pre-marked rims or tyres are used. Alternatively, the technician performing the measurement/adjustment can apply the structured markers to the wheel, but in this case the drawbacks related to the need of attaching complex equipment to the wheel are again encountered.

Other works [11, 12] proposed solutions based on laser devices projecting features to be identified on the wheel in order to perform the measurements.

These systems, however, are characterized by considerable constructional complexity and low flexibility, which is a primary issue when considering variability in vehicle and wheel dimensions.

In order to partially overcome the drawbacks of prior methods, the main aim of the present paper is to design and assess a novel Machine Vision-based system for contactless measurement of vehicles' wheel alignment. The proposed system is able to provide toe and camber angles without requiring highly precise application of

structured targets on the wheels. An appositely devised stereovision system performs a real-time acquisition of a number of non-structured near infrared (NIR) responsive markers, attached to the tyre sidewall so to describe an approximate circumference coaxial to the wheel axis. The 3D position of the markers is then related to the plane where the wheel lies by using image processing and stereoscopic triangulation-based algorithms.

The paper is structured as follows. In Section 2 the imaging acquisition hardware is described. In Section 3 the procedure for carrying out intrinsic and extrinsic calibration of acquisition devices is briefly summarized. In Section 4 the algorithms for determining 2D and 3D marker positions and wheel planes are illustrated. In Section 5 the camber and toe angle measurement procedure is provided. Finally, in Section 6 some practical results are shown and discussed.

## 2. Acquisition system

With the aim of determining the camber and toe angles of both front and rear axles of a vehicle, a proper image acquisition system has been devised.

As depicted in Figure 2, the system comprises four columns (one for each wheel) each one equipped with two commercial QXGA resolution ½ inches CMOS cameras, surrounded by an LED ring working in the NIR range (800nm). The two cameras (for each column) are placed in the upper and lower parts of the column so that their optical axes form an angle of approximately 20°. Images are acquired with a 10fps frame rate and transferred to a PC for subsequent elaboration.

Each camera is equipped with a 4.0mm f/0.8 focal length lens, possibly affected by large distortion. As is well known, many camera sensors are characterized by a slight sensitivity in the NIR range, usually attenuated by the application of an appropriate NIR filter.

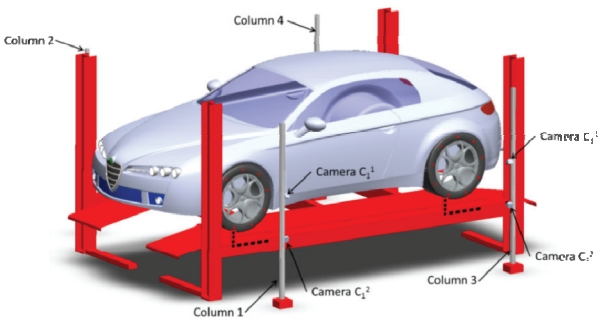


**Figure 2.** Acquisition system

Since, on the contrary, the author's idea is to specifically work in the NIR range, such a filter has been replaced by an NIR pass band filter in the range 700-900nm. As a consequence, the visible light is removed from the acquired images. The columns are placed laterally to the car lift at a distance of approximately 0.8m, so that each pair of cameras acquires a 1335 x 1000mm scene, containing a single wheel; in this configuration the spatial resolution results are equal to 0.65mm/pixel. A number (at least six) of circular (non-structured) NIR responsive markers (diameter 20mm) need to be manually placed on the tyre sidewall so that 1) the locus of marker centre points defines, approximately, a circumference coaxial with the wheel (practical tests have shown that up to a 5mm distance from the ideal circumference can be tolerated) and 2) the markers are approximately evenly spaced. This may be practically performed by adhesively placing the markers using, as a reference, one of the circular outlines, which can always be found on the tyre sidewall (see Figure 3). It must be noted that the tyres are required to be reasonably cleaned in order to avoid the markers detachment due to excessive dirt. Generally speaking, the use of such markers is preferable with respect to pre-marked plates, since they are inexpensive and cannot be damaged. Nonetheless, pre-marked plates could also be used with the proposed methodology even if in this case a very small deformation of plates (possibly due to accidental falls) could produce incorrect measurements.

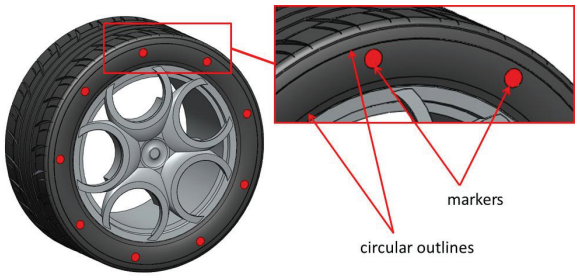


**Figure 3.** Outlines and markers on tyre sidewall

The car lift is provided with four L-shaped targets (placed in proximity to the position of the four wheels when the car is on the lift) provided with a unique NIR responsive marker (whose "negative" consists of a number of squares). Such targets, meant to work as a reference system for the evaluation of toe and camber angles, need to be placed with high precision as further explained in the next section. In the present work, the L-shaped targets are characterized by a shorter vertical arm (with respect to the horizontal one) in order to avoid possible overlapping of the wheel in acquired images. The described architecture may be used with all types of vehicle lifts, including scissors, parallelogram and two and four-post lifts to the condition that sufficient room for placing the L-shaped targets is available.

## 3. System calibration

The central issue in the set-up of the proposed stereo-vision system is two-fold: 1) determining the single

camera calibration and performing the stereo calibration of each pair of cameras equipping a single column and 2) determine the relative position of all the pairs of cameras with respect to a global coordinate system (VCS).

*3.1 Mono and stereo camera calibration*

Each of the cameras $C_i^j$ (where $i = 1...4$ is the index of the acquisition columns and $j = 1,2$ is the index of the cameras of each column) is intrinsically calibrated, independently, in order compute the focal distance and to take into account non-idealities such as lens distortion. Although a number of different calibration methods and models have been investigated by the authors [13], in the present work this procedure is performed according to the widely known approach described in [14, 15], since it proved to be the most effective in properly calibrating the system. The results of camera calibration consist of determining the following parameters:

- Camera Matrixes $KK_i^1$ and $KK_i^2$ defined, for the generic $j^{th}$ camera.
- Focal distances (a unique value in mm) $f^j_u$ and $f^j_v$ expressed in units of horizontal and vertical pixels for the generic $j^{th}$ camera.
- Coordinates of the image principal point, $u^j_0$ and $v^j_0$.
- Distortion coefficients (in the image directions x and y) for the generic $j^{th}$ camera $k^j_u$ and $k^j_v$.

Obviously, calibration procedure is affected by uncertainties on the assessment of such parameters. In order to reduce possible calibration errors, we used a checkerboard calibration pattern with the following specifications:

- maximum flatness error equal to 0.05mm;
- maximum error in dimension of the single checker equal to 0. 1mm;
- maximum error in absolute position of a single checker on the pattern equal to 0. 1mm.

Once all the single cameras are calibrated, a stereo calibration can be carried out. As is well known, the goal of a stereo calibration routine (once each single camera is accurately intrinsically calibrated) is to determine the relative position in space of the two cameras equipping a single column (stereo couple). In detail, stereo calibration allows the evaluation of:

- Rotation Matrixes $R_i^{12}$ between the reference systems of the cameras making up each stereo couple (camera 1 and camera 2 of the $i^{th}$ column).
- Translation Vectors $T_i^{12}$ between the camera 1 and the camera 2 of the $i^{th}$ column.

*3.2 Determination of the relative position of all the stereo couples with respect to the vehicle coordinate system (VCS)*

The main aim of this task is to determine the position of all the cameras in a properly defined Vehicle Coordinates System (VCS), a frame of reference usually adopted by manufacturers to specify the alignment parameters. This is possible if the position of each L-shaped target is known with respect to the others, i.e., a properly Lift Coordinate System (LCS) is defined. In such a case, the position of the four stereo couples in a common reference system can be retrieved by evaluating the local reference system of each L-shaped target with respect to one of the cameras making up each stereo couple.

First, the reference systems of each L-shaped target ($O_iX_iY_iZ_i$) need to be defined. In the exemplificative case of considering a front left target, the corresponding reference system is arranged as follows: the origin $O_1$ is identified by the centroid of the lower left quadrilateral of the marker (see Figure 4), the axes are positioned so that $Y_1$ is defined by the line passing through $O_1$ and the centroids of all the vertically aligned quadrilaterals, while $X_1$ is defined by the line passing through $O_1$ and the centroids of all the horizontally aligned quadrilaterals.

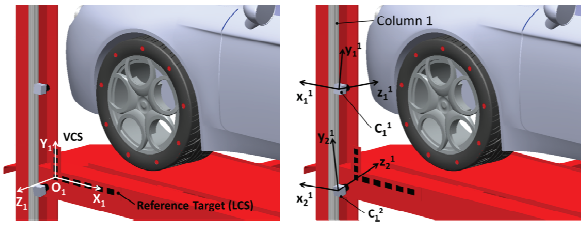


**Figure 4.** Definition of the VCS and camera reference systems

One of the L-shaped targets has to be selected for conventionally setting the VCS. From now on, the front left target reference system is selected as VCS.

Referring to column 1, the camera $C_1^1$ is able to acquire the reference target in its field of view so that a number of feature points belonging to it can be retrieved. The knowledge of such points, as explained below, allows the reference system's evaluation with respect to the camera. In acquiring the necessary images to identify the L-shaped target, though the cameras are equipped with NIR pass band filter and the marker is NIR responsive, the (non-uniform) environmental light may be responsible for undesired background noise. Moreover, noise can occur in acquired images due to possible LED light reflections. In order to remove these non-uniformities, the following procedure has been used:

An image of the target is acquired by the camera $C_1^1$ first with LED off (see Figure 5a) so that only background noise and reflections due to environmental light are visible in the image. Another image is then acquired with

LED on (see Figure 5b). Accordingly the entire scene objects (background, reflections and markers) reflected in the NIR range are visible. Finally, an image $I_1^1$ is evaluated as the difference between the image acquired with LED on and the one with LED off (Figure 5c). This allows an image where both the background noise and the reflections due to environmental light are removed to be obtained. Unfortunately, when the LED ring is turned on, reflections in the NIR range may still occur in the image. As a consequence further processing is required.

The image $I_1^1$ is processed by global thresholding using the Otzu method [16], thus obtaining a binary image $B_1^1$ where the marker, the reflections and the possible noise are described by white pixels, while both the background and the quadrilaterals inside the marker are represented by black ones (see Figure 5d).

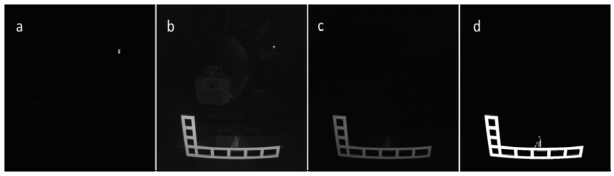


**Figure 5.** (a) image acquired with LED off; (b) image acquired with LED on; (c) difference between "LED on" and "LED off" images; (d) thresholded image

The image $B_1^1$ is processed by applying connected component labelling [17] and then the $0^{th}$ moment of each binary labelled object is computed.

Since the NIR responsive marker is the labelled object characterized by the greater area (this actually occurred in all the performed tests, also using different lifts and cars), both possible noise and NIR light reflections are removed by image $B_1^1$ by simply discarding all labelled objects whose $0^{th}$ moment is lower than the maximum one.

The resulting image $\bar{B}_1^1$ is inverted so that the negative image $\tilde{B}_1^1$ represents the projected quadrilaterals using white pixels (while the background is black).

Image $\tilde{B}_1^1$ is also processed as described in Step 3; moreover the $1^{th}$ moments of the labelled components are evaluated, so that the nine centroids of each projected quadrilateral are detected. Note that, due to the actual positioning of the vision system and the dimensions of the target, the well-known difference between the projection of the centroid and the centroid of the projection, which is induced by perspective distortions, can be neglected.

Since the nine physical centroids lie on plane $X_1Y_1$ (and their position in such a plane is known), planar homography [18] can be computed between the corresponding points in such a plane and in the image one. The homography allows the 3D position of the nine centroids to be determined, thus including the origin $O_1$. Such centroids are used for computing the least square best fitting plane. The centroids themselves are then projected onto such a plane so as to define the axes $X_1$ and $Y_1$ as follows. $X_1$ is assumed to be the best fitting line computed for all the horizontal points (including $O_1$), while $Y_1$ is defined as the best fitting line computed for vertical ones. The knowledge of $O_1$, $X_1$ and $Y_1$ allows the axis $Z_1 = X_1 \wedge Y_1$ to be determined so that the whole VCS is now known. Once the VCS is known with reference to the camera $C_1^1$, it is possible to (reversely) refer camera $C_1^1$ to it.

The same procedure described above for camera $C_1^1$ (Steps 1-7) can be reiterated for cameras $C_2^1$, $C_3^1$ and $C_4^1$. As a result, the reference systems defined by the four targets (each one expressed in the reference system stated by camera 1 of the corresponding column) are now known.

Finally, it is possible to determine the position of all the eight cameras with respect to the VCS by knowing the relative position (translation vector and rotation matrix) of the four targets attached to the car lift. Although such roto-translations are measurable with a sufficient accuracy using, for instance, 3D Scanners or other 3D measurement devices, in the present work some convenient technical solutions have been adopted in order to simplify this task. First, the L-shaped targets are attached to the car lift using inclinometers so that the $X_iZ_i$ planes are practically parallel to the ground (orientation error lower than 0.005°). In order to fix the remaining rotation and the three translations among the four reference systems, suitable mounting equipment (whose description lies outside the aim of this work) has been devised and used. The actual obtained target positioning has been, successively, validated by means of 3D scanning. Using such equipment it is possible to practically align $X_1$ and $X_2$ with $X_3$ and $X_4$, respectively and $Z_1, Z_2$ with $Z_3, Z_4$, while $\Delta X_{13}, \Delta X_{24}$, $\Delta Z_{12}$ and $\Delta Z_{34}$ (see Figure 6) are constrained by the mounting equipment with a maximum error of ±0.5mm.

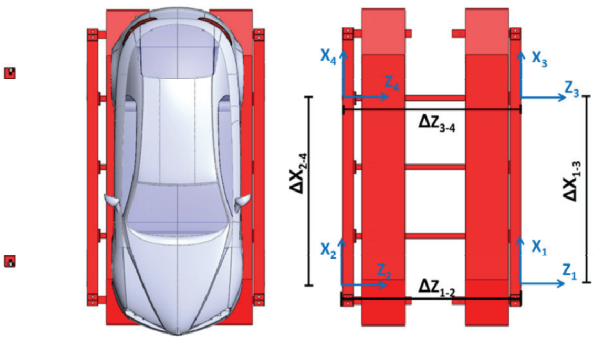


**Figure 6.** Relative position of the four targets.

As a concluding remark, it has to be noted that, since the retrieved reference systems are based on L-shaped target acquisition, the targets themselves need be manufactured with sufficient accuracy in order to guarantee measurement results are good enough. The final result of this calibration procedure is the complete knowledge of the position of any camera with respect to the LCS. This allows the acquisition columns to be moved as desired, within certain practical limits, without having to measure their movements and/or rotations with other methods. In fact, the aforesaid procedure allows automatic recalibration of external camera parameters at all times (assuming the corresponding targets are visible from the selected position of the four columns).

## 4. Wheel planes evaluation

In order to determine toe and camber angles of the four wheels, the evaluation of wheel planes is essential. As detailed in the rest of this section, such planes are determined by combining image processing based algorithms together with stereo triangulation (Figure 7). First, noise (background and reflections possibly due to chromed, polished and glossily painted surfaces) in the wheel images is partially removed. Then, the correspondence between 2D marker centroids in the images from camera 1 and camera 2 of each column is univocally determined using the procedure described in Section 4.2, regardless of the possibility of remaining noise.

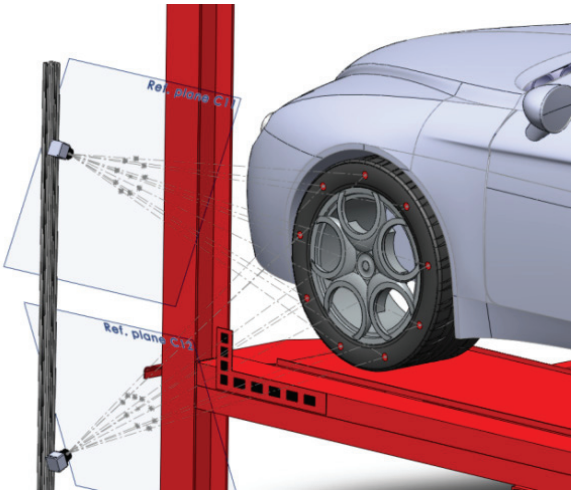


**Figure 7.** Triangulation between NIR marker centroids with respect to front left wheel

### *4.1 Noise removal from images*

Once the whole system is calibrated, the images of the four wheels can be processed. As already stated, each pair of cameras is able to acquire a single wheel. For the sake of clarity, the procedure described below is referred to as single column (images acquired by cameras $C_1^1$ and $C_1^2$); obviously, the images from the remaining three columns are processed analogously.

Similarly to the acquisition of L-shaped targets, two wheel images $J_1^1$ and $J_1^2$ are obtained as the difference between the corresponding images acquired with LED on and off.

Images $J_1^1$ and $J_1^2$ are subsequently thresholded so that only the NIR responsive markers, plus possible areas due to reflections, are visible in the resulting images. By applying component labelling and by evaluating region moments, it is possible to obtain for each image a set of $n^j$ $(j=1,2)$ connected components, each one characterized by an area $A^j_n$ and a centroid vector (2x1) $c^j_n$.

Among them, only $m < n^j$ connected components ("c.c." from now on) represent, for each image, the NIR responsive markers (where *m* is the number of markers attached to the wheel). Therefore, a procedure for removing the remaining $m - n^j$ c.c. (representing reflections) has to be defined. Since markers are round, due to perspective, they are represented in acquired images by ellipses. Depending upon the camera(s) relative position with respect to the wheel, such ellipses may be characterized by different area values even if the actual area is the same for all markers. Moreover, reflections also may result in (approximately) elliptic zones whose areas may be comparable with the ones characterizing the markers. As a consequence, detection of markers in an image is not trivial and an image processing based procedure, described below, is required for discarding most of the reflections.

1. A threshold area value $A_t$ is evaluated as the actual area of a marker $A_a$ and normalized with respect to the spatial resolution. In this work, since the marker diameter is 20mm, $A_a = 314\text{mm}^2$ and $A_t = 743.5\text{pixel}^2$. All the c.c. whose area $A^j_b$ is lower or greater than $0.5A_t$ and $1.5A_t$ respectively, are discarded. Due to perspective and wheel rotation the markers may appear as ellipses whose area is considerably different from the ideal one. As demonstrated by experimental tests, the range $[0.5A_t - 1.5A_t]$ assures a good c.c. discrimination for all the possible wheel rotations of practical interest in wheel alignment.
2. 2nd moments of c.c. are computed so that the principal axes are also computed. The ratio $\alpha^j$ between the major and minor axes is evaluated and all the c.c. for which $\alpha^j < 0.5$ and $\alpha^j > 1.5$ are discarded. The result of steps 1-2 is still a set of $\bar{n}^j > m$ connected components.
3. Unfortunately, although $\bar{n}^j < n^j$, the procedure described above does not always allow the removal of all possible reflections in acquired images. The remaining reflection induced c.c. (r.i.c.c.) can be

removed by means of additional processing, as described in Section 4.2.

*4.2 Correspondences evaluation and triangulation*

In order to properly detect correspondences between c.c. acquired by each camera of a given stereo couple (and to discard the remaining r.i.c.c.) epipolar geometry is used. With reference to column 1, epipolar lines are computed for the $\bar{n}^1$ centroids detected in image $J_1^1$ according to [19]. As is well known, such lines should pass perfectly through the centroids of the corresponding points in image plane $J_1^2$. Actually, due to both numerical and (possible) calibration errors, the epipolar lines pass "near" the corresponding points. Therefore, a criterion for determining point-to-point correspondence between c.c. in images 1 and 2 needs to be used. In the present work the correspondent points (i.e., the pair of marker centroids in images 1 and 2 defining the actual marker centroid in the 3D space) are determined using an Euclidean distance based procedure: first, the set *S* of all points whose Euclidean distance from the epipolar line is lower than a threshold value $\varepsilon$ (set in the present work to equal to 20 pixels) is created; then, the following scenarios are possible (see Figure 8):

- The epipolar line originated from a marker centroid in image $J_1^1$ passes near one marker centroid (i.e., *S* is composed by only one marker centroid); as a consequence, such a point is the only one univocally satisfying the epipolar constraint (see for instance epipolar lines *e1*, *e2*, *e4*, *e5*, *e6*, *e7* and *e8* in Figure 8) and the point to point correspondence is determined.
- The epipolar line originated from a marker centroid in image $J_1^1$ passes near two (or more) marker centroids (i.e., *S* is composed by two or more marker centroids); in this case, one of the points composing the set *S* is surely the correspondent one.
- The epipolar line originated from a marker centroid in image $J_1^1$ passes near one (or more) marker centroid(s) and one (or more) r.i.c.c.
- The epipolar line originated from an r.i.c.c. in image $J_1^1$ passes near two (or more) marker centroids; for instance the epipolar line *en1* in Figure 8.

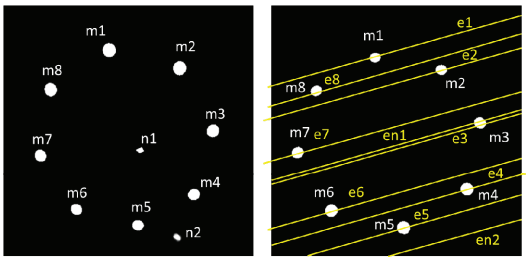


**Figure 8.** (a) detection of centroids – marker m and noise n - on image $J_1^1$; (b) corresponding epipolar lines on image $J_1^2$

- The epipolar line originated from an r.i.c.c. in image $J_1^1$ passes near one (or more) marker centroid(s) and one (or more) r.i.c.c.
- The epipolar line originated from an r.i.c.c. in image $J_1^1$ passes near two (or more) r.i.c.c. This is a very rare case since the light reflection due to LED illumination is nearly perpendicular to the LED ring; so the LED reflections hardly occur in the same point framed by the two cameras.

For all the described scenarios the discrimination of corresponding points is still required since epipolar constraint does not provide univocal results. Hence, the following strategy was adopted:

1. All the centroids (marker and/or r.i.c.c.) detected by the generic epipolar line are stored and used for 3D triangulation according to [20]. The triangulation result consists of a set of $h$ 3D points (with $h \neq \bar{n}^j$) usually composed by a number of points greater that $m$; among them only $m$ points represents markers and are appropriate for evaluating wheel plane.
2. For the set containing $h$ elements, the number of its distinct three-element subsets is evaluated by using the binomial coefficient $\binom{h}{3}$.
3. For each three-element subset the equation of the plane (through three points) is evaluated. The result is a set of $h' = \binom{h}{3}$ planes. Among them, the $m' = \binom{m}{3}$ planes defined by centroid markers are characterized by similar normal vectors values. For instance, in Figure 9 the marker centroids lie on a number of planes (in red) while other planes (in magenta) are defined by wrong correspondence detection.

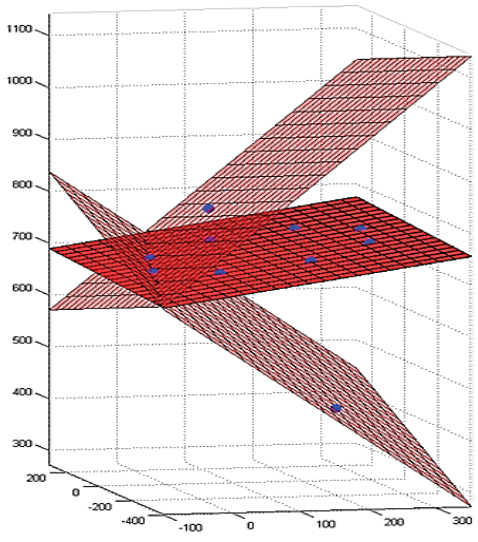


**Figure 9.** Planes defined by marker centroids (in red) and planes defined by marker and noise centroids (in magenta)

In order to detect these planes, the absolute value of the dot product for all the possible permutations of the pairs of normal vectors for the $h'$ planes is evaluated. The $m'$ planes are the ones whose dot product is nearly equal to one. Consequently, all the pairs of planes whose absolute value of the dot product results is greater than 0.95 may be considered a reliable guess of the wheel plane. In fact, this procedure allows the user to get rid of the possibly remaining reflections spots from the pre-processing described in Section 4.1.

4. Finally, the wheel plane is evaluated as the least square-fitting plane approximating the points that define the $m'$ planes. Approximation to the minimum squares is used to reduce the effect of possible errors related to marker misplacement. Using an appropriate number of points (at least six) it has been demonstrated by experimental tests that this kind of error is drastically reduced, so that the validity of the measurement is not nullified. In case a lower number of markers are used, the wheel plane equation is obviously still obtained (three points are strictly necessary) but results can be excessively prone to the error affecting the measurement of each single point, thereby producing an unreliable result.

## 5. Toe and camber measurement

The procedure described in Section 4 allows the determination of the equation of the four wheel planes, each one referred to the $C_i^1$ of the respective acquisition column. Since the positions of all the cameras are known in the VCS, it is forthright to refer all the wheel planes to the global coordinate system. In detail, toe angle is provided by:

$$\psi = \arcsin\left(\left\|v_i \wedge v_z\right\|\right) \cdot \frac{180}{\pi} \tag{1}$$

Where $v_i$ is the normal vector for the $i^{th}$ wheel and $v_z$ is the normal vector of the plane $X_1Y_1$.

Analogously, the camber is defined as follows:

$$\vartheta = \arcsin\left(\left\|v_i \wedge v_y\right\|\right) \cdot \frac{180}{\pi} \tag{2}$$

Where $v_y$ is the normal vector of the plane $X_1Z_1$.

The toe angles defined in Eq. 1, do not take into account possible misalignments of the car with respect to the car lift. In order to compensate for this effect, an additional step is required. Since the wheel marker centroids approximately define a circumference in the 3D space (coaxial to the wheel axis) it is possible to evaluate the wheel centre coordinates with respect to the VCS as the centre of the 3D best fitting circumference. Once the 4 wheel centre coordinates are known, the lines connecting the four centres define a quadrilateral as shown in Figure 10. The thrust axis deviation, i.e., the axis defining the misalignment of the vehicle, is evaluated as the line joining the midpoints of the front and rear part of the quadrilateral. Finally, the angle $\psi'$ defined by the thrust axis deviation and the $X_1$ axis is used for compensating the run-out effect (i.e., to evaluate the actual toe $\psi''$) as follows:

$$\psi'' = \psi + \psi' \tag{3}$$

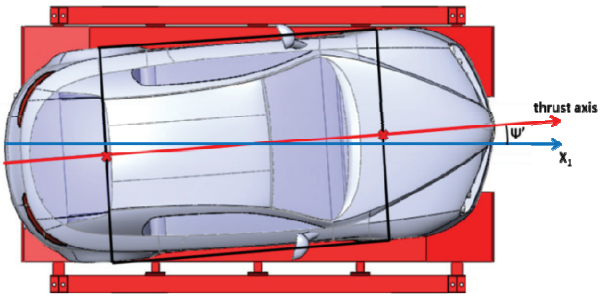


**Figure 10.** Run-out effect due to misalignment of the vehicle

## 6. Results and conclusions

With the aim of assessing the correctness of toe and camber measurement provided by the devised system, measurement results were tested against a complete 3D reconstruction of wheel alignment obtained using a commercial 3D scanner (Romer Absolute Arm 7520). The scanner is a seven axis portable CMM for dimensional inspection, it is equipped either with a completely integrated high-performance laser scanner or with a touch probe so it allows both optical and tactile measurement.

Laser scanning accuracy is declared equal to 0.058mm using the full measurement range (approx. 4m). In the worst case, such an accuracy may lead to a maximum error in determining wheel angles equal to 0.009° when measuring a 14'' wheel; since wheel alignment is considered accurate when the measured angles are affected by an error not exceeding 0.05°, the 3D scanning measurement can be considered to provide sufficiently accurate values to be compared with the ones coming from the proposed apparatus. The device has been used for 3D scanning of a Toyota Yaris, provided with 14'' wheels and placed on a car lift. Three acquisitions have been carried out setting different toe and camber angles of the four wheels. It has to be noted that, since the front vehicle wheels are set on two translating support platforms (which can always be found on car lifts and are meant to allow front wheel steering), by changing the toe and camber angles of the four wheels, the thrust axis changes too. For all configurations, toe and camber have been measured using the proposed machine-vision system. The resulting values are compared with the ones obtained by processing the point clouds resulting from the 3D scanning (see for instance Figure 11).

In detail, starting from a generic point cloud, wheel planes have been evaluated by best fitting the centroids of all the NIR markers (each centroid is, in turn, evaluated as the barycentre of all the points composing each marker). By means of the same procedure, the target planes have been evaluated using the centroids of the quadrilaterals inside the L-shaped target. Finally, toe and camber angles have been assessed using Eq.1-3 after referring all the planes (wheels and targets) to the VCS. Results listed in Table 1 show that the absolute average difference between the angles measurement using the 3D scanner and the same obtained using the proposed machine vision system is equal to 0.024° and to 0.026° for toe and camber, respectively.

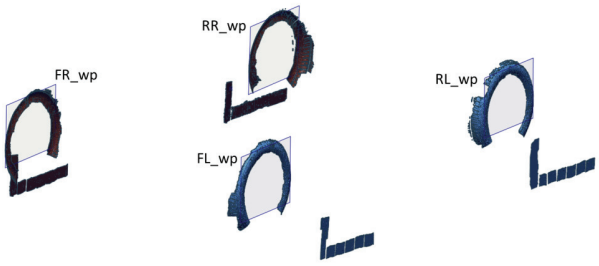


**Figure 11.** Point cloud resulting from 3D scanning process.

In other words, the system provides measures with an absolute difference lower than 0.05° with respect to the 3D scanner measurement. Accordingly, the described MV system proves to be effective for toe and camber measurement for the considered test case.

| N° | Wheel | Angle | 3D Scanner | MV System | Absolute difference |
|---|---|---|---|---|---|
| Test 1 | FL | Toe | 0.144 | 0.124 | 0.020 |
| | | Camber | -0.236 | -0.253 | 0.018 |
| | FR | Toe | 0.353 | 0.366 | 0.013 |
| | | Camber | -0.646 | -0.622 | 0.024 |
| | RL | Toe | 0.297 | 0.281 | 0.016 |
| | | Camber | -0.439 | -0.411 | 0.028 |
| | RR | Toe | 0.301 | 0.326 | 0.026 |
| | | Camber | -0.447 | -0.482 | 0.035 |
| Test 2 | FL | Toe | 0.175 | 0.195 | 0.020 |
| | | Camber | -0.204 | -0.227 | 0.023 |
| | FR | Toe | 0.313 | 0.328 | 0.015 |
| | | Camber | -0.603 | -0.642 | 0.039 |
| | RL | Toe | 0.257 | 0.236 | 0.021 |
| | | Camber | -0.374 | -0.399 | 0.025 |
| | RR | Toe | 0.267 | 0.234 | 0.033 |
| | | Camber | -0.387 | -0.339 | 0.048 |
| Test 3 | FL | Toe | 0.096 | 0.134 | 0.038 |
| | | Camber | -0.157 | -0.186 | 0.029 |
| | FR | Toe | 0.202 | 0.181 | 0.021 |
| | | Camber | -0.464 | -0.442 | 0.022 |
| | RL | Toe | 0.198 | 0.159 | 0.039 |
| | | Camber | -0.326 | -0.343 | 0.017 |
| | RR | Toe | 0.167 | 0.144 | 0.023 |
| | | Camber | -0.298 | -0.277 | 0.021 |
| **Average difference** | | | | | **0.026** |
| **Average difference toe** | | | | | **0.024** |
| **Average difference camber** | | | | | **0.027** |
| Legend: FL, RL: front and rear left wheels. FR, RR: front and rear right wheels. | | | | | |

**Table 1.** Comparison between toe and camber measurements performed using the 3D scanner and the MV system.

Further work will be addressed to perform additional validation taking into consideration a number of different vehicles in order to spot possible issues related to errors introduced by manufacturing tolerances in rims and wheels, damage to the wheel assemblies and to suspension components, mounting variances of tyres onto the rims and deformation of the gantry under the vehicle weight. Moreover, practical usage scenarios will be investigated to test the robustness of the system versus the variability induced by human factors.

Future work will also be addressed to the reduction of the number of stereo couples necessary to perform the measurement. From this point of view, the possibility of using only two columns (one for each car side) moving on a linear track will be investigated as well as the option of using a single stereo pair for simultaneously observing two wheels.

## References


[1] Zhang YY, Liu MS, Luo FG, Wang JR (2004) Research of measurement technology and performance appreciation of the automobile four-wheel alignment instruments. China Measurement Technology. Available: http://en.cnki.com.cn/Article_en/CJFDTOTAL-SYCS200404000.htm.

[2] Díaz V, Ramírez M, Muñoz B (2004) A wheel model for the study of the wheel angle measurement in the periodic motor vehicle inspection. International Journal of Vehicle Design. 34(3): 297-308.

[3] Pacejka HB (1973) Simplified Analysis of Steady-State Turning Behaviour of Motor Vehicles Part 3: More Elaborate Systems. Vehicle System Dynamics. 2(4): 185-204.

[4] Furukawa Y, Yuhara N, Sano S, Takeda H, Matsushita Y (1989) A Review of Four-Wheel Steering Studies from the Viewpoint of Vehicle Dynamics and Control. Vehicle System Dynamics. 18(1-3): 151-186.

[5] Jackson BF (2000) Method and apparatus for determining the alignment of motor vehicle wheels. US Patent 6,148,528.

[6] Healy DA (2009) Two-wheel alignment adjustment method. US Patent 7,532,742.

[7] January DB (1998) Apparatus and method for determining vehicle wheel alignment measurements from three dimensional wheel positions and orientations. US Patent 5,724,128.

[8] Li W, Gao Y, Zhang R (2011) Research on the Machine Vision System for Vehicle Four-wheel Alignment Parameters. Proceedings of the 30th Chinese Control Conference. July 22-24, Yantai, China.

[9] Wang D, Tu Y, (2007) An approach to measuring vehicle four-wheel alignment parameters based on computer vision. Proceedings of The 8th International Conference on Electronic Measurement and Instruments ICEMI'2007, August 16-18, Xian, China.

[10] Jackson DA (2006) Wheel aligner measurement module attachment system. WO Patent 2006124642.
[11] Uno H (1998) Wheel alignment measuring instrument and wheel alignment measuring. US Patent 6,412,183.
[12] Downing EA (1991) Light scanning system for measurement of orientation and physical features of a workpiece. US Patent 5,054,918.
[13] Furferi R, Governi L, Nunziati M (2011) On the performance of several stereo calibration methods and models. Proceedings of International Conference on Innovative Methods in Product Design, Improve 2011, San Servolo, Venice (Italy), June 15th – 17th, 2011, 416-422.
[14] Weng J, Cohen P, Herniou M (1992) Camera Calibration with Distortion Models and Accuracy Evaluation. IEEE transactions on pattern analysis and machine intelligence. 14: 965-981.
[15] Clarke TA, Fryer JG (1998) The Development of Camera Calibration Methods and Models -, Photogrammetric Record. 16(91): 51-66.
[16] Otsu N (1979) A threshold selection method from gray-level histograms. IEEE Trans. Sys, Man., Cyber. 9(1): 62–66.
[17] Samet H, Tamminen M (1988) Efficient Component Labeling of Images of Arbitrary Dimension Represented by Linear Bintrees. IEEE Transactions on Pattern Analysis and Machine Intelligence, 10: 579.
[18] Agarwal A, Jawahar CV, Narayanan PJ (2005) A survey of planar homography estimation techniques. Technical report, IIT-Hyderabad.
[19] Papadimitriou DV, Dennis TJ (1996) Epipolar line estimation and rectification for stereo images pairs. IEEE Trans Image Process 3(4): 672–676.
[20] Choi BK, Chin HY, Loon YI, Lee JW (1988) Triangulation of scattered data in 3D space Comp. Aided Geom. Des. 20: 239–248.